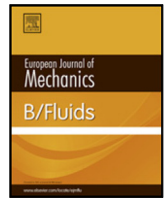




Contents lists available at ScienceDirect

European Journal of Mechanics / B Fluids

journal homepage: [www.elsevier.com/locate/ejmflu](http://www.elsevier.com/locate/ejmflu)

## Discussion on instabilities in breaking waves: Vortices, air-entrainment and droplet generation

Pierre Lubin<sup>a,\*</sup>, Olivier Kimmoun<sup>b</sup>, Fabrice Véron<sup>c</sup>, Stéphane Glockner<sup>a</sup>

<sup>a</sup> Université de Bordeaux, Bordeaux-INP, I2M UMR CNRS 5295, 16 avenue Pey-Berland, 33607 Pessac, France

<sup>b</sup> Aix-Marseille Université, Institut de Recherche sur les Phénomènes Hors Équilibre (IRPHE), UMR CNRS 6594, Technopôle de Château-Gombert, 49 rue Joliot Curie, 13384 Marseille Cedex 13, France

<sup>c</sup> School of Marine Science and Policy, College of Earth, Ocean and Environment, University of Delaware, Newark, DE 19716, USA

### ARTICLE INFO

Article history:  
Available online xxxx

Keywords:  
Navier–Stokes  
Numerical simulation  
Experimental visualizations  
Instabilities  
Breaking waves  
Splash-up  
Air entrainment  
Vortices

### ABSTRACT

When waves are breaking, several instabilities are observed to be responsible for several features, like vortices, air-entrainment and droplets generation. Being able to ascertain if the number and sizes of droplets during breaking events can be controlled by instabilities and in which order these perturbations lead to droplets production, is evidently of great interest. Thanks to some numerical simulations and new experimental visualizations, a discussion is proposed to analyze the successive steps of atomization of a plunging liquid jet when a wave break. The complexity of the phenomenon will be highlighted, while some possible instability mechanisms will be described. Following the plunging jet impact, vortex filaments are produced, inducing air entrainment and complex structures which can be similar to the so-called obliquely descending eddies.

© 2018 Elsevier Masson SAS. All rights reserved.

### 1. Introduction

Recent numerical works revealed greater physical details on turbulent structures and yielded insight on air entrainment, bubbles generation processes when waves break [1–6]. The consensus among all the authors however, is that the finest features of the flow prove challenging to both model and explain.

As stated by van der Meer [7], an instability “is a phenomenon in which the liquid spontaneously changes its shape and/or appearance”. Many flows can be subjected to a single type of instability, with only one wavelength or narrow-banded disturbance present on the interface. But most of real flows, like breaking waves, are subjected to multiple types of co-habiting instabilities, where several wavelengths and frequencies of flow disturbances can occur simultaneously and with competing growth rates. Classical Kelvin–Helmholtz (KH) and Rayleigh–Taylor (RT) instability theories have been widely used in the context of spray formation [8] and atomization [9]. If droplets generation is a response to an instabilities during wave breaking events, this immediately leads to the challenging question: What is(are) the source(s) of the instability(ies)? Thus, the details of the droplets

generation process are likely to be dependent on the surface tension, viscosity, density, and diameter of the plunging jet undergoing breakup. Villermaux [9] described the mechanisms responsible for the transition between a liquid volume and its subsequent dispersion into stable drops, showing that “primary instabilities always give birth to more or less corrugated ligaments whose breakup determines the shape of the drop-size distribution in the resulting spray”. Examples were examined to show that “drops come from the rupture of objects in the form of threads or ligaments”.

Being able to ascertain if the number and sizes of droplets during breaking events can be controlled by instabilities and in which order these perturbations lead to droplets production, is evidently of great interest. The ultimate goal would be to deduce a physically based model depending on parameters such as the diameter, length and spacing of the fingers/ligaments and droplets, as time advances during a single breaking event. In the present contribution, we wish to further analyze the numerical results presented by Lubin and Glockner [3] in order to describe the change of topology of the free-falling plunging jet, and having described its kinematics, we will discuss candidate processes potentially responsible for several interfacial features (scars, air entrainment and droplets generation). It is acknowledged that surface tension is not modeled, but the numerical results are solely used to illustrate the discussion about the multiple instability mechanisms occurring when waves break. Wave breaking can still be seen as a very complex and multi-parameter problem that can hardly be

\* Corresponding author.

E-mail addresses: [pierre.lubin@bordeaux-inp.fr](mailto:pierre.lubin@bordeaux-inp.fr) (P. Lubin), [olivier.kimmoun@centrale-marseille.fr](mailto:olivier.kimmoun@centrale-marseille.fr) (O. Kimmoun), [fveron@udel.edu](mailto:fveron@udel.edu) (F. Véron), [glockner@enscbp.fr](mailto:glockner@enscbp.fr) (S. Glockner).

<https://doi.org/10.1016/j.euromechflu.2018.05.006>

0997-7546/© 2018 Elsevier Masson SAS. All rights reserved.

decomposed into simple hydrodynamic features. We have an overturning jet accelerating and then fragmenting as it free-falls down, exhibiting a curved shape, resulting into a large mass of water impacting, splashing and exploding into numerous bubbles and droplets. We will thus restrict this manuscript to descriptions and discussions about plausible scenarios, without quantifying phenomena that would undoubtedly be affected by surface tension. We will thus discuss and frame the successive steps of atomization of a plunging liquid jet when a wave break, as simply as possible as we felt that there was a need for basic discussion looking at the gist of the phenomenon. We will then present some new experimental visualizations in order to discuss air entrainment and vortical structures generated beneath breaking waves.

## 2. Description of the numerical model

### 2.1. Governing equations

In this paper, we present further analysis of the results from the numerical simulations performed to describe the generation of filament vortices [3]. Therefore, the governing equations and numerical methods will only be briefly summarized here, further details can be found in [3]. We solved the Navier–Stokes equations in air and water, using the Large Eddy Simulation (LES) framework. The resulting set of equations describing the entire hydrodynamic and geometrical processes involved in the motion of non-miscible multiphase media is given by Eqs. (1)–(3) below:

$$\nabla \cdot \mathbf{u} = 0 \quad (1)$$

$$\rho \left( \frac{\partial \mathbf{u}}{\partial t} + \mathbf{u} \cdot \nabla \mathbf{u} \right) = -\nabla p + \rho \mathbf{g} + \nabla \cdot ((\mu + \mu_t) [\nabla \mathbf{u} + \nabla^t \mathbf{u}]) \quad (2)$$

$$\text{and} \quad \frac{\partial C}{\partial t} + \mathbf{u} \cdot \nabla C = 0 \quad (3)$$

where  $\mathbf{u}$  is the velocity,  $C$  the phase function used to locate the different fluids,  $t$  the time,  $p$  the pressure,  $\mathbf{g}$  the gravity vector,  $\rho$  the density,  $\mu$  the dynamic viscosity. The turbulent viscosity  $\mu_t$  is calculated with the Mixed Scale model [10].  $x$ ,  $z$  and  $y$  are respectively the horizontal, vertical and transverse coordinates.  $u_x$ ,  $u_z$  and  $u_y$  are the corresponding velocity components of the velocity vector  $\mathbf{u}$ . The surface tension is not considered in this study, as discussed by Lubin and Glockner [3]. The numerical results are solely used for illustration purposes, in order to discuss the multiple instability mechanisms occurring when waves break. The real air and water physical properties are used, the magnitudes of the physical characteristics used in the numerical simulations are given in Table 1.

In order to have an accurate description of the free-surface motion, the interface tracking is achieved by a Volume Of Fluid method (VOF) and a Piecewise Linear Interface Calculation (PLIC) [11,12]. The numerical tool has already been shown to give accurate results for environmental and industrial applications [13–16]. All the details of the numerical methods used to discretize and solve the Eqs. (1)–(3) are given in Lubin and Glockner [3].

Surface tension forces computation is still an active and challenging research field. With VOF-PLIC like methods, curvature is given by a second derivative of the volume fraction, or alternately, of the height function built from the volume fraction [17]. But PLIC methods are, at best, second order in space. Thus, curvature computation verifies an  $O(0)$  convergence order. This assessment can be verified with the “advected” Laplace test case of the equilibrium between pressure and surface tension forces of a fluid disk that is advected in a uniform velocity field [18–20]:

- if the disk is not advected (static case), curvature is converging at second order only if the volume fraction is initialized exactly or with enough precision (see fig. 1 in [20]).
- if the disk is advected, one loses this precision on the volume fraction due to the error induced by the advection scheme (that is only second order), and curvature does not converge [19,20].

An option consists in using higher order interface representation and transport methods, like Level Set/WENO5 for example, that gives curvature computation convergence order at least equal to two [20]. But they are not free of deficiencies (mass conservation, redistanciation) that makes it not suitable for breaking wave simulations. Instead, we would hybrid method CLS-VOF that takes advantage of both methods for further works. But this work is now in progress.

We used a parallel version of the code, which allowed us to run simulations with high grid density. More than 100 millions of mesh grid points have been used to discretize the three-dimensional numerical domain ( $1024 \times 500 \times 200$ ), with non-uniform mesh grid cells. The grid was evenly distributed in longitudinal and transverse directions ( $\Delta x = \Delta y = 10^{-4}$  m). In the vertical direction, the grid was clustered with a constant grid size  $\Delta z = 10^{-4}$  m in the free-surface zone. The three-dimensional numerical domain has been partitioned into 1024 subdomains (one processor per subdomain). The computing time was approximately 24 h, with 1024 cores, for a simulated physical time of 0.88 s.

### 2.2. Initial and boundary conditions

The initial conditions corresponded to a single unstable periodic sinusoidal waves of large amplitude, with initial quantities calculated using the linear theory. With this method, the overturning motion is controlled by two initial parameters, the initial steepness,  $H/L$ , and the dispersion parameter,  $d/L$ , where  $d$  is the water depth,  $H$  the wave height and  $L$  the wavelength. This approach is quite interesting because we are then able to study any breaker type by varying only these simple flow parameters [21–23,13,24,3,4].

In the following, we further describe the plunging breaking wave simulated with  $H/L = 0.13$ ,  $d/L = 0.13$  which corresponds to the configuration presented by Vinje and Brevig [21]; this allows for easier validation and comparison of the velocity and acceleration fields [25].

## 3. Results and discussion

### 3.1. Overturning motion and general flow description

The general processes involved in the wave steepening and subsequent breaking event are now well known and have been fully described by numerous authors including complete reviews by Peregrine [26] and Kiger and Duncan [27].

In shoaling water, as it approaches the beach and because of the decreasing water depth, the propagating wave become asymmetric. The forward face of the wave steepens and a plunging jet is eventually projected forward from the crest of the wave. As the face of the wave becomes vertical, three main features of the overturning motion, located in three different regions of the steepening wave have been reported [28–31,26,32]:

- high water-particle velocities are found at the crest of the steepening wave. From this well known observation, the most commonly accepted criterion to identify the beginning of the plunging breaking process is when the maximum horizontal velocity component magnitude becomes greater than the wave celerity, or a fraction thereof;

**Table 1**  
Physical parameters used for the 3D numerical simulations by Lubin and Glockner [3].

Water density, $\rho_w$	1000 kg m <sup>-3</sup>	Water viscosity, $\mu_w$	$1 \times 10^{-3}$ kg m <sup>-1</sup> s <sup>-1</sup>
Air density, $\rho_a$	1.1768 kg m <sup>-3</sup>	Air viscosity, $\mu_a$	$1.85 \times 10^{-5}$ kg m <sup>-1</sup> s <sup>-1</sup>
Gravity, $g$	9.81 m s <sup>-2</sup>	Surface tension	Neglected

- (ii) high water-particle accelerations are located on the forward face of the wave. The acceleration field is directed from the water towards the air. The high water accelerations exceed the acceleration of gravity;
- (iii) the particles on the rear of the wave have both low and a negative horizontal accelerations.

At the initial time of the simulation, the water velocity field in the wave was obtained from the linear theory and the air was quiescent. The wave propagates towards the right side of the periodic domain and the free-surface shape becomes increasingly asymmetric. The front face of the crest then steepens and becomes vertical. At the instant  $t = 0.28 T$  s (Fig. 1), a good agreement is found between our simulation and the Boundary Integral Element Method computation of Vinje and Brevig [21] (see Figs. 4 and 5 from original authors). Vinje and Brevig [21] found that the maximum acceleration magnitude, at  $t = 0.28 T$  s, is located on the face of the wave and is about 2.4 g. This value is compared with maximum acceleration magnitude of 2.3 g obtained in the present simulation. Interestingly, the maximum of acceleration is located on the under side of the overhanging jet and is directed out of the fluid, towards the air. They also indicated that the horizontal velocities at the wave crest are slightly larger than the phase velocity. The initial wave celerity is  $c = 0.324$  m s<sup>-1</sup>. The present computed maximum horizontal velocity is about  $u_x = 0.351$  m s<sup>-1</sup>. As expected, a high velocity region is found in the impinging jet.

The projected jet of water free falls forwards, following a nearly ballistic trajectory, as previously checked [3] compared with the approximation given by Drazen et al. [33] for the vertical velocity of the toe at impact on the surface.

The plunging breaking wave is then responsible for the generation of jet-splash cycles. Large scale coherent counter-rotating and co-rotating vortices are then observed. While the work presented by Lubin and Glockner [3] was focused on the vortex filaments generated underneath the plunging breaking impact, looking further at some small details of the flows yields some interesting insight on particular features at the interface. At various stages of the breaking process, several interfacial and vortical structures can be observed, some of which have been partially explained by other authors while some phenomena are still open to debate.

### 3.2. Droplets generation

When a body of water is ejected and free-falls down as a planar jet, it can be subjected to several hydrodynamic instabilities which are summarized hereafter.

- [34] Rayleigh–Taylor (RT) instability is a buoyancy-driven which occurs when a high density fluid is accelerated in a low density fluid. As it is inertia-driven, it becomes less effective when deceleration occurs.
- Kelvin–Helmoltz (KH) instability is driven by velocity shear and occurs in a continuous fluid system where velocity shear is present or between two fluids due to a sufficient velocity difference across the interface.
- Plateau–Rayleigh (RP) instability describes the phenomenon where a falling jet or cylinder of fluid at one point ceases to be a jet and breaks into multiple droplets of smaller total surface area due to surface tension.

- Richtmyer–Meshkov (RM) instability is shock-induced and occurs due to the interaction between a shock wave and an interface separating two fluids. As the shock penetrates the interface, positive/negative pressure perturbations near the crests/troughs of the interface cause the instability to grow, similar to Rayleigh–Taylor instability.
- Görtler vortices are a form of three-dimensional secondary flow that appear in a boundary layer flow along a concave wall [35]. These streamwise-oriented counter-rotating vortices are due to centrifugal acceleration.

Prior to the plunging jet impact, several researchers have reported on the presence of interfacial striations on the back of the free-falling planar jet [36–38,4]. It is commonly accepted that these striations are due to counter-rotative subsurface vortices. Wang et al. [4] speculated that these could be due to the presence of Görtler vortices, as can be seen in cascades [39]. As reported by Wang et al. [4], instabilities analysis in plunging wave breaking is difficult as many complex processes and phenomena are involved.

We present the wave breaking process in Figs. 2 and 3, as matching pictures of sky and front views. The wave is propagating towards the right side of the periodic numerical domain, moving out on the right side to re-enter on the left side. As soon as the jet starts developing and showing a curved profile, the striations become clearly visible. A closer look is provided for the early process of the jet ejection in Fig. 4.

The plunging jet follows a ballistic motion and it is usually observed that the jet of water ejected from the wave crest expands and its extremity fragments into droplets. The process of fragmentation of the plunger can be split up in a sequence of instabilities. The Rayleigh–Taylor (RT) and Kelvin–Helmholtz (KH) instabilities are two of the most studied instability mechanisms. The RT instability is known to occur in the presence of a density stratification in an acceleration field. On the other hand, the KH instability, is known to occur due to a velocity difference across an interface. But fragmentation of interfaces is a very complex multi-parameter problem. The physical mechanisms which are responsible for the generation of the droplets are still not fully determined as multi-stage instability mechanisms can be observed depending on the physical phenomenon (drops impacts, jet atomization, liquid sheets, etc.) [9].

Droplets are observed to be generated at several stages of the plunging breaking events. When the plunging jet is ejected, droplets can be observed to be formed at the top of the crest (Fig. 4). When the jet is free-falling down and about to impact, the tip can also be observed to be torn into small droplets. When the jet impacts and the subsequent splash-up develops, more droplets can also be produced. Various elongated structures appear as seen in Figs. 2 and 3. Tiny fingers or ligaments are seen in various stages of the breaking event, which then break into very small isolated cylinders and droplets. A ligament is a more or less columnar object attached by its base to the liquid from which it has been stripped. The droplets are typically very small and their sizes seem to be dictated by the radius of the ligaments. With time, the length scales of these ligaments are observed to increase as they can be flapping and stretching, instead of remaining constant. The common process we present in Fig. 5 is the generation of these liquid ligaments, following different instabilities development. Again, it must be kept in mind that the numerical results have been obtained without taking surface tension into account and the pictures are solely proposed for illustration purposes.

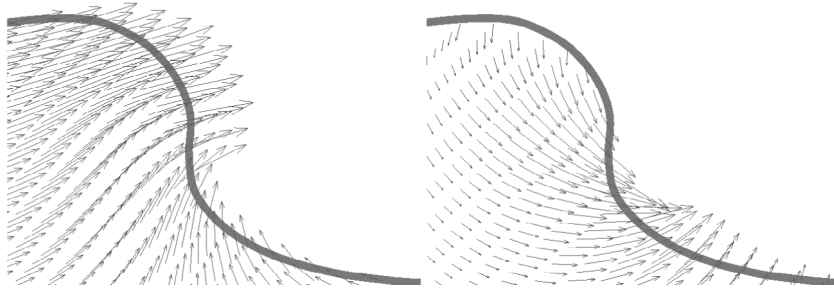


**Fig. 1.** Velocity and Lagrangian acceleration fields at  $t = 0.28 T$  s. Only one vector in four is shown in the water in the vicinity of the crest before breaking.

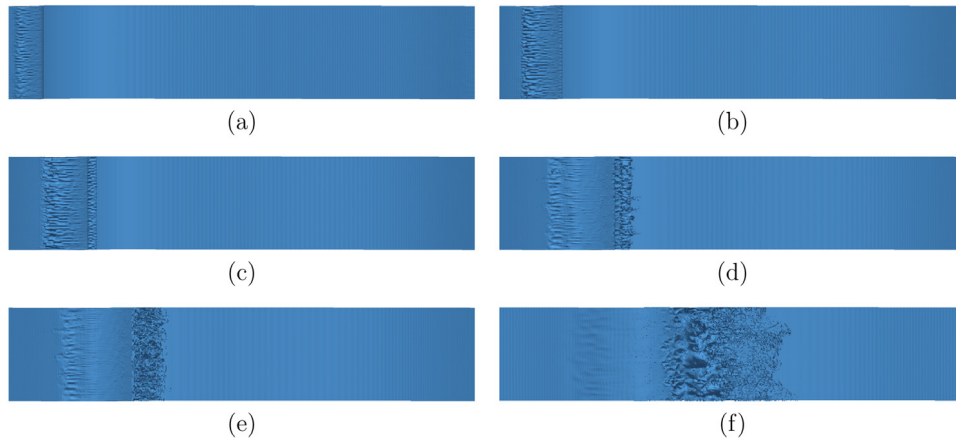


**Fig. 2.** Evolution of the plunging breaking event, view from above. The plunging breaking is initiated from picture (a) to (f).

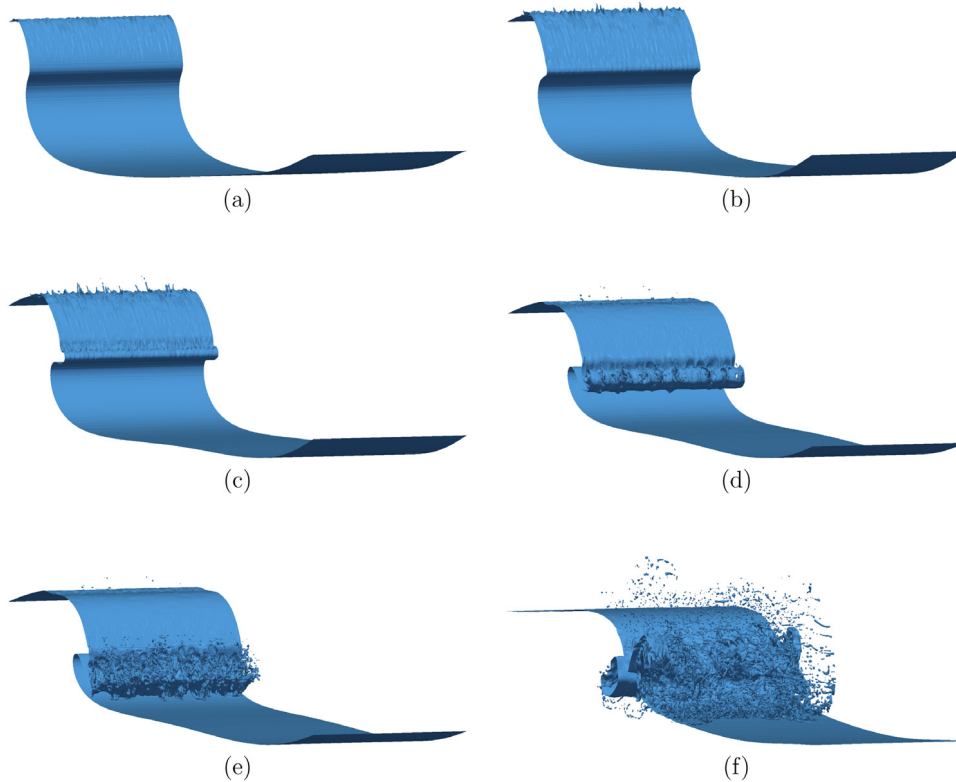


**Fig. 3.** Evolution of the plunging breaking event, view from the mean water level. The plunging breaking is initiated from picture (a) to (f), corresponding to the same instants as those presented in Fig. 2.

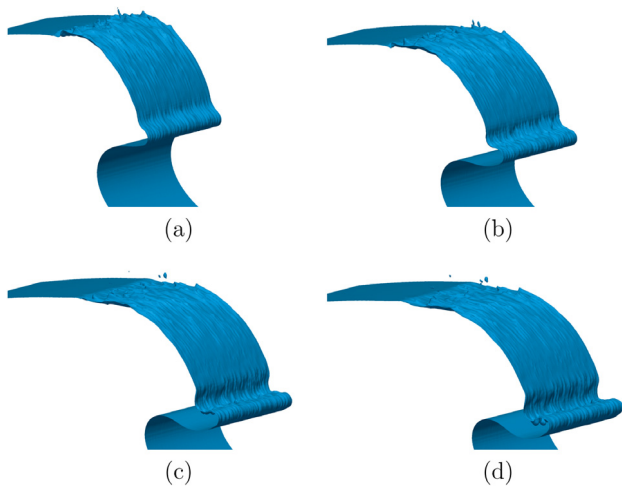


**Fig. 4.** Sequence of pictures presenting the evolution of plunging jet from its ejection at the crest. 3D strip extracted from the whole numerical domain for a clearer identification of the structures.

When looking at the crest, a primary shear instability is first triggered and followed by a RT instability of liquid ligaments produced by the primary instability. The shear instability is driven by the boundary layer of the air flow while the crest of the undulations due to the striations of the back of the jet undergo a destabilization, of a RT type, caused by the accelerations. This would mean that the plunging jet dimensions could be practically irrelevant as the instability is of interfacial nature, the process of fragmentation being only function of the boundary layer in the air flow above the crest, which would determine the wavelength of the primary instability and the subsequent fluid mass that is suddenly exposed to the air flow and accelerated. This is only hypothesized as a plausible scenario which needs to be confirmed using data or simulations that take surface tension into account. The droplets generated are mainly moving backwards and are almost immediately falling due to the gravity. As we do not consider wind, the droplets are not advected far from their source. Moreover, modeling surface tension would have surely affected the interfacial processes and the subsequent droplets generation.

Subsequently, the plunging jet develops. It can be seen as a heavy liquid (water) inter-penetrating a lighter one (air), thereby triggering a RT instability along its rim. Indeed, the shape of the tip of the plunger is not rectilinear, and a transverse wavelength can be observed, and which is longer than the striations observed on the back of the plunging jet. Then a KH instability can occur as a secondary instability during this growth, modifying the tip of the plunger prior the impact. The tip of the jet can be viewed as the cat-eye formations along the side of RT spikes [34]. It reveals the importance of surrounding air as illustrated in Fig. 5. As the tip of the jet free-falls down, air is entrapped and attempts to escape from the pocket about to be closed. The water jet can then be destabilized due to the velocity gradient (shear) between the surrounding air and the liquid tip. When the KH instability grows, ligaments can be observed and initiate the atomization in small droplets. The droplet generation can thus be described as a series of instabilities. Initially, as the primary KH instability developing at the tip of the plunging jet, followed by a secondary RT instability at the interface of the accelerating liquid ligaments. The liquid ligaments can also interact with the surrounding air flow and develop a KH instability, conferring to the ligament a flapping motion.

Once the jet impacts and the splash-up is projected forward, another sequence of liquid ligaments generation can be observed.

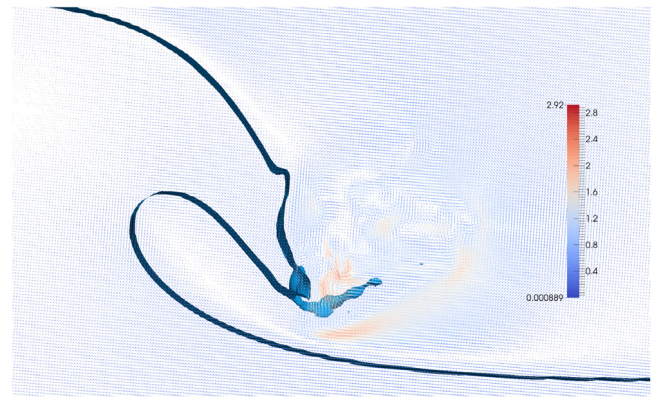


**Fig. 5.** 3D strip extracted from the whole numerical domain for a clearer identification of a ligament formation at the tip of the plunging jet. The free-surface is identified with the isocontour of the phase function  $C = 0.5$  (in blue). Velocity vectors indicate the flow direction and its intensity. (For interpretation of the references to color in this figure legend, the reader is referred to the web version of this article.)

Ligaments are also observed to be generated by disintegration of holes in liquid sheets between ligaments (Fig. 3(d) and (e)).

All these ligaments grow rapidly and are exposed to, and accelerated by, the surrounding air flow. Interacting with the surrounding turbulent air, ligaments exhibit irregular shapes and complex dynamics when they break into droplets. Being then able to identify which instability is responsible for the size of the final droplets mechanism is of importance in order to be able to propose a model for spray generation. From the observations considered here, it is not clear if the disintegration of the ligaments in droplets is finally due to another instability. Indeed, ligaments can simply be torn off by the air flow or another longitudinal instability may occur while the ligaments are stretched and elongated. The disintegration of a longitudinally expanding ligament could either be due to local acceleration induced by flapping when the friction with the surrounding air is strong enough to trigger KH instability, or solely due to the RT (acceleration-driven) or RP (surface tension-driven) mechanism, which causes cylindrical liquid forms to break into droplets. Ligaments then can produce final drop sizes which can be larger than their thickness, due to coalescence between the blobs that make up a ligament [8].

Once the plunging jet has impacted, the splash-up is generated as a secondary planar jet projected upward and forward Watanabe et al. [38], Saruwatari et al. [40]. Looking at Figs. 2 and 3, it can be seen that several wavelengths of different instabilities co-exist, all leading to filaments and droplets ejection. Every kinks and wrinkles observed on the free-surface of the plunging event can give birth to ligaments, under the influence of unstable KH velocity gradients. It can also be speculated that the impact of the plunging jet could produce a RM instability, the shock generating ligaments in the splash-up as observed when drops impact on a liquid film [41]. But no clear evidence of a RM instability overcoming a more plausible RT instability mechanism can be given.

Despite their role in air-water momentum, heat and moisture fluxes, with known implications in the development of tropical storm systems, the generation of water droplets by breaking waves and the subsequent transport of this sea spray in the marine atmospheric boundary layer is a problem that is still poorly understood.

Sea spray droplets are generally classified according to their perceived generation mechanism. Small spray droplets of radii  $O(0.01) - O(200) \mu\text{m}$  are ejected from the surface when bubbles, previously injected in the water column by the breaking process, rise to the surface and burst. This surface bubble bursting process in turn generates drops when the bubble cap shatters,

the film drops of radii  $O(0.01) - O(1) \mu\text{m}$  and the jet drops of radii  $O(2) - O(200) \mu\text{m}$  when the leftover cavity collapses and generates a central jets that fractionates. Large spray droplets, called spume drops, are believed to be formed when the wind is sufficiently strong to mechanically tear off water particles from the top of waves. Evidently, spume droplets are also generated in the absence of wind in which case they quickly fall back without being transported in the atmospheric boundary layer. The extent to which wind shear is a dominating factor or simply influences the generation process is still undetermined. In short, the spume generation process, the details of which are still largely unknown, generates particles of radii  $O(20) - O(3000) \mu\text{m}$  [42,43].

For oceanographic and meteorological applications, the drop source function (the flux of drops) rather than the number size distribution, is usually required to estimate relevant air-sea fluxes. Thus, the pertinent quantity is the number of spray droplets of radius  $r$  generated at the ocean surface per unit surface area per unit time. However, direct measurements of the drop source function are challenging and estimates are therefore rather scarce. This is especially true for the spume droplets, which cannot be easily captured in the field by conventional fixed-height measurement techniques because their residence times are short, keeping some of them within a wave height of the surface.

Thus, parameterizing the drop source function for the large drops ejected from breaking front is of great interest, but a knowledge of the physical mechanisms involved is usually preferred.

Experiments were performed in the high-speed Plexiglas wind-wave tank at the university of Delaware (see Veron et al. [44] for details). In order to acquire reliable drop size distributions, high resolution images in the along-wind plane were taken using a digital SLR photo camera. This configuration allowed for the detection of drops with radii of  $90 \mu\text{m}$  and larger. Three wind speeds of  $U_{10} = [31.3, 41.2, 47.1] \text{ms}^{-1}$  ( $U_{10}$  is equivalent 10-meter wind speed) were studied. Experiments using a high speed camera acquiring small images (1Mpix) of the wave crests at a rate of 1000 Hz we also performed. The images allowed to gain insight into the physical mechanisms responsible for spray generation at these high wind speeds. Finally, wind and wave measurements were performed using a Pitot tube and optical wave gauge respectively. The wind speed profiles provided extrapolated  $U_{10}$  values, the friction velocity,  $u_*$ , and drag coefficient,  $C_D$ .

By processing the high resolution images, the droplet spectral concentration functions  $dC/dr$ , i.e. the number of drops per  $\text{m}^3$  of air per radius increment, were constructed for radii of  $90 \mu\text{m}$  to  $2750 \mu\text{m}$ . These experimental results indicate that the drop number concentration scales between  $dC/dr \sim r^{-3}$  and  $dC/dr \sim r^{-5}$  for the larger drops. The measured drop concentrations also show a substantial number of supra millimeter size drops, size at which surface tension ceases to be relevant. In addition, these large drops were significantly larger than the Hinze scale, the size at which turbulent breakup dominates the fractionation process (i.e. the drop radius at the critical Weber number, Hinze [45,46,47]). Surprisingly perhaps, no clear regime change in the distribution is evident at that scale. This suggests, perhaps not surprisingly, that surface tension may have a limited influence on the spray generation at the scale of these rather large droplets. Large droplets were also observed in the laboratory experiments of Anguelova et al. [48] and Fairall et al. [49].

Interestingly, using the high speed imagery, [44] observed the formation of elongated globules or filaments on the front face of a breaking wave. Even under the influence of the wind, a number of these filaments are reminiscent of the feature described above and shown on Figs. 9 and 12. These filaments subsequently break up into a number of daughter droplets as outlined above. Furthermore, the high speed observations revealed a previously overlooked spray generation mechanism. On the breaking front of

a wave, the bursting of so-called lenticular canopies were observed (see Villermaux and Bossa [50]). These are inflated by the wind and burst creating a large number of droplets. While this phenomenon is unlikely to occur at low wind speeds, it may be a frequent occurrence in high winds with strongly forced waves. However, these preliminary data only cover a reduced range of wind-wave conditions and clearly, further investigation of this generation mechanism is needed.

The globule and ligament breakup processes outlined above are the basis for the modeled generation function of Mueller and Veron [51] which we briefly described below.

Succinctly, based on the work of Marmottant and Villermaux [8], [51] developed a spray generation function which assumes that spray from breaking front sheared by the wind are first ejected along breaking wave crests in the form of globules (or ligaments). These ligaments then break up under in the turbulent airflow over the wave crest; the breakup model is based on the Hinze scale and does not consider filament breakup under KH instabilities as discussed above.

The modeling result are in general agreement with spray mass loading and spray-mediated air-water momentum fluxes. However, the model fails to reproduce the large drops observed in the experiments described above [44]. Evidently, this stems from the fact that the model relies on turbulent breakup (Hinze scale) which is not supported by the observation of large drops. It is possible that the turbulent breakup in the model is erroneously estimated because our knowledge of the turbulent airflow field over the waves is still incomplete [52]. Indeed, the turbulent kinetic energy dissipation upon which the estimate of the Hinze scale relies, can quickly vary by order of magnitudes over short distances in the vertical direction in the presence of a moving free surface and (breaking) waves. It is also possible that these drops fall back before having been appreciably exposed to the turbulent airflow and thus before the breakup process takes places.

Another possible explanation for the discrepancy is that the spray generation mechanism, for the large drops, might not heavily rely on the breakup of ligaments by the turbulent airflow, but might instead be controlled by a more fundamental inertial process. Indeed, the simulations presented above, as well as recent simulations of mechanical breaking waves by Wang et al. [4] (in the absence of wind) show the generation of significant spray during the splash-up. The spray size distribution from the simulations of Wang et al. [4] agrees remarkably well with the data of [44] (which were taken in high winds and presumably in conditions that do not yield plunging-type breaking waves).

Clearly, the physical mechanisms responsible for the formation of spray droplets by breaking waves are not well resolved and need to be studied in more details, both numerically and experimentally.

### 3.3. Air entrainment

Most of the recent works have been dedicated to the description of the complicated three-dimensional vortical structures generated beneath breaking waves [1,53,6,54], namely the “obliquely descending eddies” [55]. Vortical structures, called vortex filaments, were described under plunging breaking waves and found to be responsible for some air entrainment [3]. Very limited number of similar observations could be found (see Table 2). Their lateral distribution at generation seemed to be driven by the striations found on the back of the plunging jet. However, we shall examine the evolution of these vortex filaments after inception. Indeed, we believe that their evolution can bring further insight into the physics of the so-called obliquely descending eddies (ODE). While the vortex filaments formation has been numerically confirmed by the works of Brucker et al. [56] and Wang et al. [4], the air entrainment in the core of the filaments was not observed in these

**Table 2**

Summary of experimental pictures available in the literature showing the air entrainment in vortex filaments. All configurations showed plunging breaking events.

References	Figures	Observations
Lamarre [57]	Figure 3.11, pictures 26 to 30 (page 98)	Experimental underwater pictures showing “air penetration” and “finger-like structures”
Deane and Stokes [58]	Figure 5	Underwater observations in a natural location, also discussed by Deane and Stokes [59]
Rojas and Loewen [60]	Figures 2b and 12	Filaments of air observed around the main air cavity generated after the plunging jet impact
Brucker et al. [56]	Figure 4	Numerical simulation showing vortices, but no air entrainment in the cores
Blenkinsopp and Chaplin [61]	Figure 8	Experimental work using tap water
Blenkinsopp and Chaplin [62]	Figure 3	Experimental work comparing air entrainment as a function of water type (freshwater, artificial seawater or natural seawater)
Lim et al. [63]	Figures 5 (c) to (e)	Experimental images detailing the plunging breaking process from the first plunging jet impact to the second splash-up
Wang et al. [4]	Figures 6	Numerical simulation showing vortices, but no air entrainment in the cores

simulations and the subsequent evolution of the vortical structures is not shown. Further investigations of these structures is thus required.

Looking at Fig. 6 from Wang et al. [4] which depicts the  $Q$ -criterion in order to identify the 3-D vortex structures, we can see that the Görtler vortices are not visible in the plunging jet. The same is true of the figures presented in [3]. Thus, the  $Q$ -criterion does not allow to see the Görtler vortices, if they are indeed present. So, the mechanism responsible for the striations found on the back of the plunging jet and ultimately responsible for aerated vortex filaments remains elusive. When looking at vortex filaments identified by the  $Q$ -criterion presented by Lubin and Glockner [3] and Wang et al. [4], the regularity of their distribution is striking, especially when considering that they originate from a jet impact and that they exist in a highly chaotic flow. Most of the filaments are filled with air in their cores, but not all of them. Their presence are also manifested by the striations visible when they interact with the wall of the tube of air entrained by the plunging jet impact.

Looking more closely at the velocity field below the free-surface allows to see saddle points (Fig. 6). One is located at the impact of the plunging jet and has been explained to be responsible for the generation of the vortex filaments, due to a stretching and intensification process in the strain region. But another saddle point is visible under the wave crest, separating two flow regions, as explained previously: a high velocity region on the right side and a low velocity region below the back of the wave. The arrows presented on the picture show the flow directions. Part of the flow feeds the plunging jet, while the flow wrapping around the main air pocket circulates upward towards the saddle point and is again redirected in the plunging jet. The low velocity region is also divided in two parts, pointing backward.

The evolution of the coherent vortical structures underneath the plunging breaking gives also more insight about the fate of these vortical structures while they are wrapping around the main tube of air. The filaments are observed to coil while they are rising towards the saddle point beneath the wave crest. Then they form a buckle, and the loop is bending and redirecting backwards and downwards like an ODE (Fig. 7). This description is in agreement with the results from Watanabe et al. [38], Zhou et al. [1], [53], Zhou et al. [6] or LeClaire and Ting [54]. However, the simulations (and observations) cannot determine if the vortices exhibited a preferred direction for the swirling motion nor any specific alternating pattern. In order to address these questions, new experimental visualizations have been performed; preliminary results are presented hereafter.

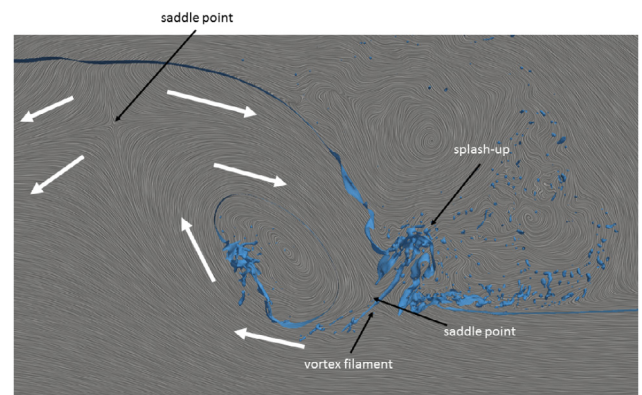


**Fig. 6.** Picture a 3D strip extracted from the whole numerical domain for a clearer identification of a single vortex filament. The free-surface is identified with the isocontour of the phase function  $C = 0.5$  (in blue). The Line Integral Convolution, calculated in the 2D plane ( $xz$ ), is displayed. The celerity of the initial wave is subtracted to the longitudinal velocity component to be in a frame-of-reference moving with the wave. (For interpretation of the references to color in this figure legend, the reader is referred to the web version of this article.)

### 3.4. Experimental setup

Experiments were performed in the wave flume at Ecole Centrale Marseille (ECM), Marseilles, France. The flume length is 16.77 m and the width is 0.65 m. The water depth during the campaign was fixed to  $h = 0.517$  m. To generate waves a flap type, hydraulically driven wave-maker is installed at one end and to absorb the incoming waves an adjustable sloping porous (8% porosity) mesh beach suspended into the tank is installed at the other (see Fig. 8).

To generate a breaking wave a classical space-time focusing technique is used. The technique start from an amplitude spectrum, in our case, a modified Ricker Spectrum, which corresponds to the second derivative of the Gaussian function:

$$a(\omega) = A\sqrt{T} e^{-\omega^m} (1 - a_p(\omega^m T - 1))$$

with  $\omega$  the pulsation,  $A$  the amplitude of the wave at the focusing distance,  $m$  and  $T$  parameters to adjust the shape of the spectrum and  $a_p$  correlated to the peak frequency by:

$$\omega_p = e^{\frac{1}{m} \ln\left(\frac{1+2a_p}{a_p T}\right)}$$

The spectrum is modified, as classically  $m = 2$  and in the present case  $m < 2$  has been chosen instead. Using  $m = 2$ , the last wave

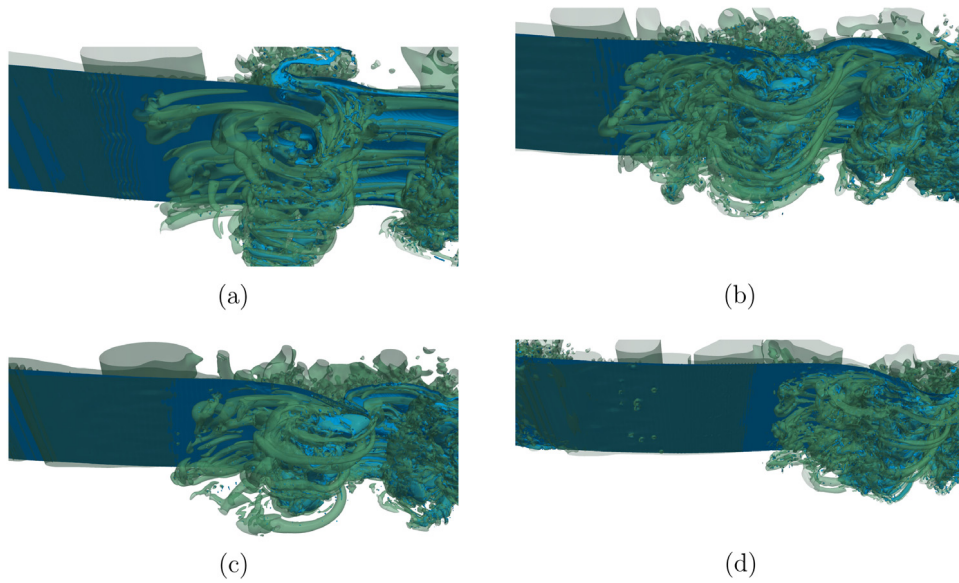


Fig. 7. Examples of vortex filaments generated for some of the 3D breaking waves simulated [3]. (a)  $H/L = 0.10$ ,  $d/L = 0.10$ ; (b)  $H/L = 0.13$ ,  $d/L = 0.11$ ; (c)  $H/L = 0.13$ ,  $d/L = 0.13$ ; (d)  $H/L = 0.17$ ,  $d/L = 0.14$ .

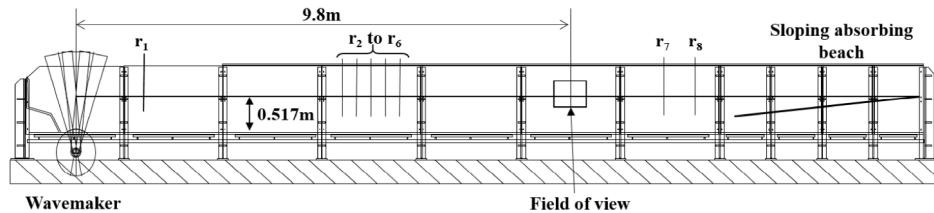


Fig. 8. Schematic presentation of the wave tank and the associated experimental setup.

of the generated group corresponds to a too large motion of the wavemaker, which is not the case for  $m = 1.5$ . This choice allows to generate more powerful focused waves with the mechanical limitations of the wavemaker [64].

The wave elevation  $\eta(x, t)$  and the flap rotation  $\theta(x, t)$  at a given focusing distance  $x$  are given by:

$$\begin{cases} \eta(x, t) = \int_{\omega} a(\omega) e^{i(\omega t - k(\omega)x)} \\ \theta(x, t) = \int_{\omega} \frac{a(\omega)}{C(\omega)} e^{i(\omega t - k(\omega)x)} \end{cases}$$

with  $C(\omega)$  the transfer function of the wavemaker and  $k(\omega)$  the wavenumber given by the linear dispersion relation. For a given focusing distance  $X_f$ , the wave elevation and the flap rotation are obtained. Then the time is reversed as  $t \rightarrow -t$  (see Fig. 9). This condition is then applied to the wavemaker.

Wave profiles were measured by a set of resistance wire wave gauges. Eight wave gauges were installed along the tank as shown in Fig. 8.

The visualizations are performed using a high speed camera with a  $2560 \times 1600$  pixel<sup>2</sup> resolution and with a frame rate of 1000 frames/second. The typical size of images is  $38.80 \times 24.25$  cm<sup>2</sup>. The distance between the wavemaker to the center of the field of view is 9.8 m. To allow a better contrast of images, a white semi-transparent screen is illuminated from behind with four LED lamps of 6000 lumens each. Two camera positions are used, one corresponds to the optical axis perpendicular to the vertical frame of the wave tank (A position), and the second with an angle of 30 degrees to allow the visualization of the back face of the wave (see Fig. 10).

### 3.5. Experimental conditions

For the A position, the position perpendicular to the vertical frame, four focusing distances  $X_f$  are considered: [9.2, 9.4, 9.5, 9.6] m. These distances corresponds to the distance from the wavemaker to the incipient breaking. Because it is difficult to move the camera with the light system and because the view area is bounded by the frames of the wavetank, instead, we shift the focusing distance in order to observe, at the fixed instrument location, the breaking evolution from the incipient breaking to the end of the first splash-up. This evolution takes place over more than one meter. To ensure that for different focusing distance the generated waves are the same, repeatability needs to be achieve. This repeatability is discussed in a next section. For each distance, three different amplitudes  $A$  were considered: [23.77, 24.85, 25.93] cm.

For the B position, the position that allows to see the back face of the wave, two focusing distances  $X_f$  are considered: 9.2 m and 9.4 m. For each distance, five different amplitudes  $A$  were considered: [23.77, 24.85, 25.93, 27.01, 28.09] cm. Each condition is repeated once in order to understand the variability of the studied phenomena.

#### 3.5.1. Experimental results

Results from the A position are first displayed for one amplitude  $A = 24.85$  cm. In Fig. 11, three snapshots at different instants for the four different focusing distance are displayed. By changing the focusing distance, all the breaking evolution can be observed. The breaker corresponds to a plunging case, with the entrapment of an air pocket. When the crest hits the free surface, a splash-up occurred. At the same time the entrapped air collapse creating a strong mix of air and water. On the left image of Fig. 12 a zoom

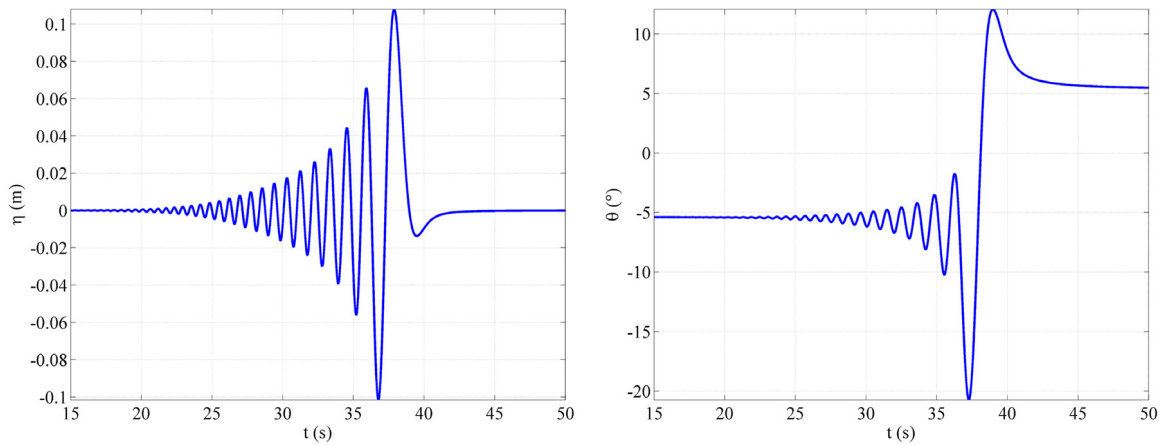


Fig. 9. (Left) Free surface elevation in front of the wavemaker, (Right) associated signal for the wavemaker.

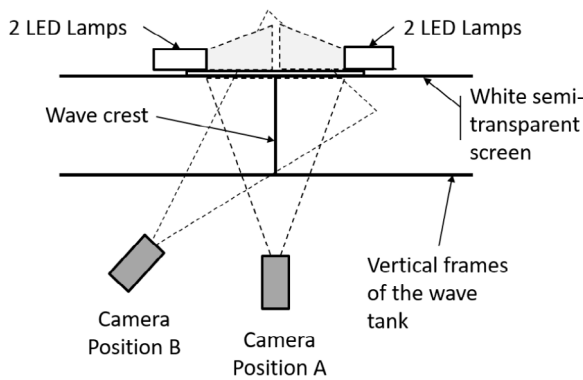


Fig. 10. (Left) Wave elevation, (Right) Flap rotation.

a periodic shape. This instability could have a major importance in the initiation of the vortices studied here after. However even if the inner part of the wave is subjected to instabilities, the outer part still very stable as it possible to observe for  $X_f = 9.40$  m on the Left image.

The middle and right images of Fig. 12 display two snapshots for almost the same instant, for 2 different amplitudes respectively  $A = 24.85$  cm and  $A = 25.93$  cm. This example shows that increasing slightly the amplitude allows to obtain really more powerful breakers. This change is visible with the size of the splash-up that increases between  $A = 24.85$  cm and  $A = 25.93$  cm.

The B position is used to observe the back face of the wave. With this view angle, it is very difficult to control the shape of the breaking waves. But due to the highly repeatability of the test for the global flow, the results showed for the A position are the same as the B position. To be convinced by the repeatability, the time evolution of the free surface at three different wave gauges for two same wave conditions is displayed in Fig. 13.

In Fig. 14, three snapshots at three different instants for  $A = 24.85$  cm and for B position are displayed. The left image corresponds to the time just after the crest impacts the free surface.

of the upper left image of Fig. 11 is displayed. It is interesting to observe that an instability occurs just behind the crest inside the tube. This instability seems, at the first stage of its initiation, to have

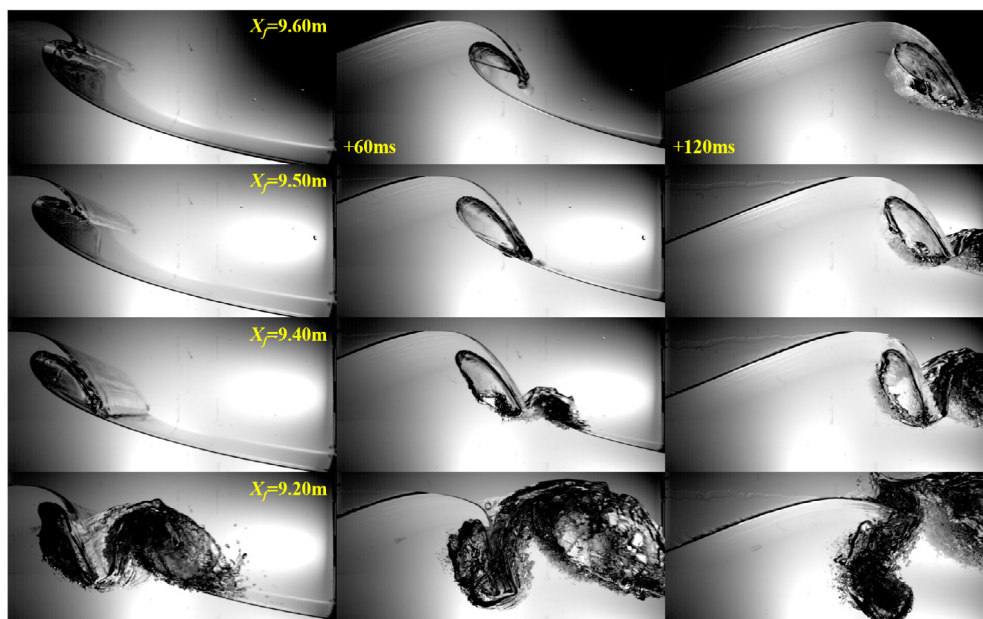
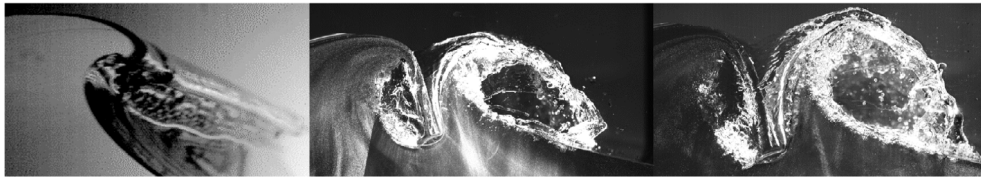
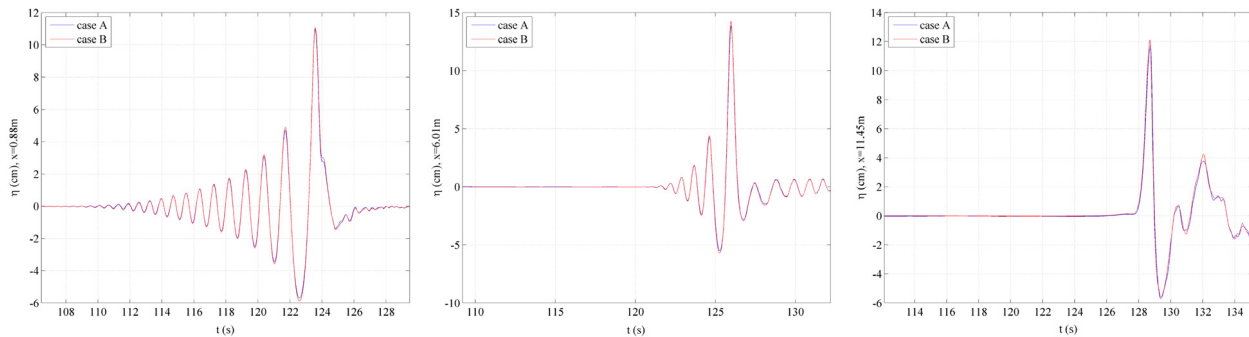


Fig. 11. Snapshots for  $A = 24.85$  cm for different focusing distance at different instants. The time for the second column is 60 ms after the first one and the time for the third column is 120 ms after the first one.



**Fig. 12.** (Left): zoom corresponding to the upper left image of Fig. 11 (Middle and Right): Two Snapshots for  $A = 24.85$  cm and  $A = 25.93$  cm.



**Fig. 13.** Time evolution of the free surface for two same wave conditions. (Left)  $x = 0.88$  m, (Middle)  $x = 6.01$  m, (Right)  $x = 11.45$  m.



**Fig. 14.** Three snapshots at three different instants for  $A = 24.85$  cm.

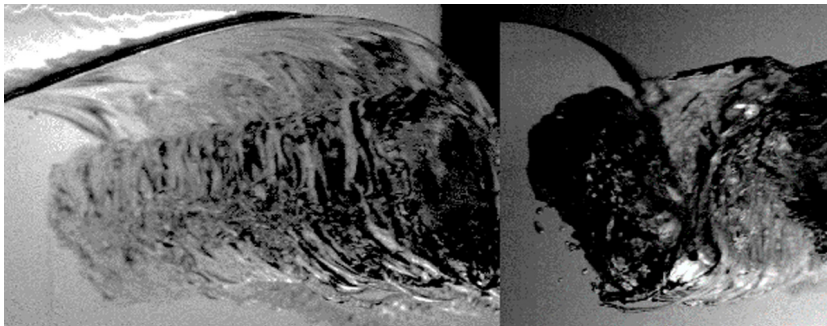


**Fig. 15.** Left: rear view for  $A = 23.77$  cm, Right: front view for the same amplitude.

This impact is followed by the growth of turbulence just under the surface. The middle image corresponds to the development of the splash-up. The turbulence limited in the previous image to the area around the impact is now visible all around the air pocket. The last image corresponds to the evolution of the splash-up and the compression of the air pocket. In this image, vortex filaments appear. The filaments follow the shape of the air pocket and the distribution seems to be irregular.

The Fig. 16 presents a close view of the vortex filaments for two equal wave conditions, for  $A = 24.85$  cm. The image on the right corresponds to a zoom of the right hand side image of Fig. 14. This figure allows us to understand that the distribution of vortex filaments is not constant for a same wave conditions, even if the initial flow conditions are exactly the same. However it seems that

the number of the most visible vortex filaments, the more energetic ones, is globally conserved. The estimation of the distance between vortices from the image database is not obvious. For the two examples displayed here ( $A = 24.85$  cm and  $A = 25.93$  cm), the number of separate visible vortices in the rear view is about seven to eight vortices. With the distance between the two vertical frames of the wave tank equal to 65 cm, the distance between visible vortices is about seven to eight cm. But attention must be paid because a part of the vortices generated at the crest are not visible in the rear view. An example is shown in Fig. 15. On the left figure is displayed the rear view for the case  $A = 23.77$  cm. In this case, only 2 or 3 vortices are visible. On the right figure, for the same case but for a front view, many vortices are visible. It means that part of the vortices generated at the crest are disintegrated before

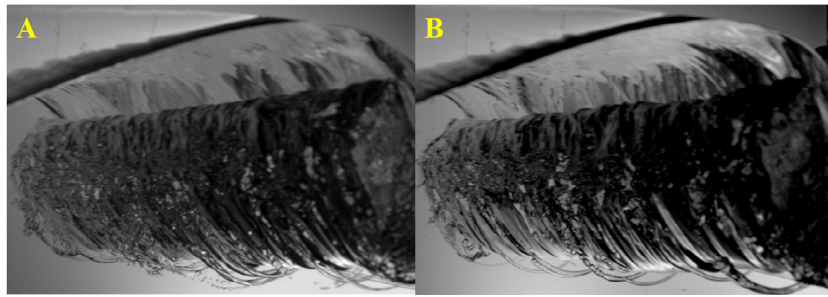


Fig. 16. Close view on the vortex filaments for 2 tests with  $A = 24.85$  cm.

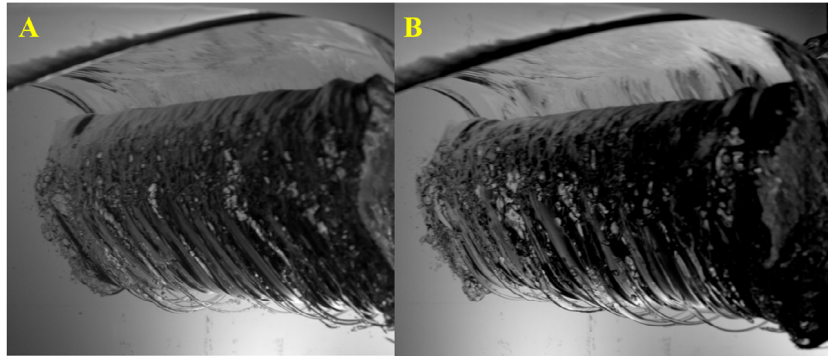


Fig. 17. Close view on the vortex filaments for 2 tests with  $A = 25.93$  cm.

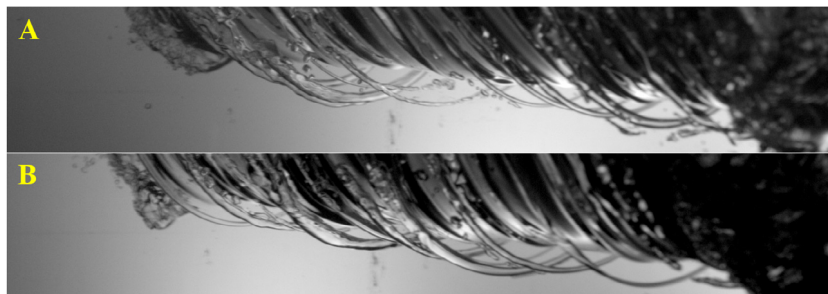


Fig. 18. Zoom on the vortex filaments for the 2 tests with  $A = 25.93$  cm.

they reach the rear part of the wave. Various mechanisms can lead to the disintegration of the vortices as instabilities or dissipation. Because the diameter of the vortices seems higher for the higher wave amplitudes, the lifetime of the vortices are higher when the amplitude increases.

The Fig. 17, is similar to the previous one but for  $A = 25.93$  cm and Fig. 18 corresponds to a closest view to better understand the distribution of the vortices. Again the distribution of filaments is not the same between the case A and the case B, but the number seems to be globally conserved.

Results for  $A = 27.01$  cm are not displayed but increasing the amplitude involves that the number of vortex filaments decreases, with only four filaments visible. This can highlight the mechanism of the initiation of instabilities at the crest, in our case with the space–time focusing technique, which tends to decrease when the amplitude of the wave increases.

The Fig. 19 can highlight the initiation of the vortex filament generation. On the left image, it is possible to observe a small filament, that is extended on the right image, when the breaking wave propagates. The filament seems to start from the root of the splash-up jet and then because the velocity of the upper part of the

breaking wave is higher than the lower part, the end of the filament wraps around the air pocket.

Even if air is sucked in the cores of some filaments, the presence of more structures can be identified by the regular striation pattern visible of the wall of the tube of air entrained by the plunging jet impact. This is very similar to the numerical observations described previously.

#### 4. Conclusions and perspectives

The wave breaking process has been discussed on the basis of numerical and experimental visualizations. The Rayleigh–Taylor (RT) and Kelvin–Helmholtz (KH) instabilities are two of the most studied instability mechanisms. The RT instability is known to occur in the presence of an unfavorable density stratification in an acceleration field. On the other hand, the KH instability, is known to occur due to a velocity difference across an interface. These two instabilities can be possibly observed at different stages of the wave breaking event: plunging jet ejection, plunging jet development and disintegration, plunging jet impact and splash-up occurrence. Ligaments can be observed before breaking into

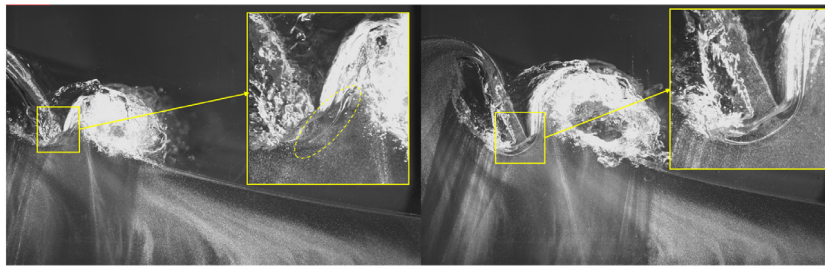


Fig. 19. Zoom on the vortex filaments for the 2 tests with  $A = 25.93$  cm.

very small isolated cylinders and droplets. Instability modes which can occur simultaneously are of major interest. KH instability often occurs as a secondary instability during the intermediate stages of RT instability growth.

Like traditional primary atomization processes (e.g. jet atomization), the plunging liquid jet is destabilized due to the relative velocity between the surrounding air flow and the free-falling water sheet, thus relying on the KH instability. But the plunging liquid jet experiences transient acceleration when free-falling down, suggesting that a RT type of instability is triggered at the jet tip, producing liquid ligaments which further stretch in the air flow and break into droplets. When the flapping liquid ligaments grow, secondary RT mechanism can be triggered due to their motion in the air flow. The possibility of using both RT and KH mechanisms simultaneously as equal contributors to the primary destabilization process has to be investigated. The final break-up of a longitudinally expanding ligament could either be due to local acceleration induced by flapping when the friction with the surrounding air is strong enough to trigger KH instability, or solely due to the RT (acceleration-driven) or RP (surface tension-driven) mechanism, which causes cylindrical liquid forms to break into droplets.

Taking surface tension into account in future simulations is required to go further into the analysis of plausible instability mechanisms. This paper is only limited to discussing potential scenarios which could lead to droplets generation, as we are only interested in highlighting plausible candidates, compared to previous works. Evaluating and measuring physical quantities needs surface tension. Finally, we wish to deduce a physically based model depending on parameters such as the diameter, length and spacing of the fingers/ligaments and droplets, as time advances during a single breaking event. Future works will be dedicated to the simulation of the new experiments described in this discussion paper. Vortex filaments are clearly very complicated to investigate. Measuring and tracing back in time the whole process responsible for the generation of these rather small structures is a challenge.

## Acknowledgments

The present article is based on work presented at the B'Waves 16 workshop in Bergen, Norway. The authors wish to thank Henrik Kalisch for organizing the conference. The authors wish to thank the Aquitaine Regional Council for the financial support towards a 432-processor cluster investment, located in the I2M laboratory. This work was granted access to the HPC resources of CINES, under allocation 2013-x2012026104 made by GENCI (Grand Equipement National de Calcul Intensif), and PRACE-RI (Partnership for Advanced Computing in Europe Research Infrastructure), MAPAV project (Massively Parallel Navier–Stokes Solver for Air/water environmental flows). Computer time for this study was also provided by the computing facilities MCIA (Mésocentre de Calcul Intensif Aquitain) of the Université de Bordeaux and of the Université de Pau et des Pays de l'Adour.

## References

- [1] Z. Zhou, J. Sangermano, T.-J. Hsu, F.C.K. Ting, A numerical investigation of wave-breaking-induced turbulent coherent structure under a solitary wave, *J. Geophys. Res.: Oceans* 119 (10) (2014) 6952–6973.
- [2] Y. Watanabe, D.M. Ingram, Transverse instabilities of ascending planar jets formed by wave impacts on vertical walls, *Proc. R. Soc. Lond. A: Math. Phys. Eng. Sci.* 471 (2182) (2015).
- [3] P. Lubin, S. Glockner, Numerical simulations of three-dimensional plunging breaking waves: Generation and evolution of aerated vortex filaments, *J. Fluid Mech.* 767 (2015) 364393.
- [4] Z. Wang, J. Yang, F. Stern, High-fidelity simulations of bubble, droplet and spray formation in breaking waves, *J. Comput. Phys.* 792 (2016) 307–327.
- [5] L. Deike, W.K. Melville, S. Popinet, Air entrainment and bubble statistics in breaking waves, *J. Fluid Mech.* 801 (2016) 91129.
- [6] Z. Zhou, T.-J. Hsu, D. Cox, X. Liu, Large-eddy simulation of wave-breaking induced turbulent coherent structures and suspended sediment transport on a barred beach, *J. Geophys. Res.: Oceans* 122 (1) (2017) 207–235.
- [7] D. van der Meer, Wrapping up a century of splashes, *J. Fluid Mech.* 800 (2016) 14.
- [8] P. Marmottant, E. Villermaux, On spray formation, *J. Fluid Mech.* 498 (2004) 73111.
- [9] E. Villermaux, Fragmentation, *Annu. Rev. Fluid Mech.* 39 (1) (2007) 419–446.
- [10] P. Sagaut, Large Eddy Simulation for incompressible flows - An introduction, Springer Verlag, 1998.
- [11] D.L. Youngs, Time-dependent multimaterial flow with large fluid distortion, in: K.W. Morton, M.J. Baines (Eds.), *Numerical Methods for Fluid Dynamics*, Academic Press, New-York, 1982.
- [12] R. Scardovelli, S. Zaleski, Direct numerical simulation of free-surface and interfacial flow, *Annu. Rev. Fluid Mech.* 31 (1999) 567–603.
- [13] P. Lubin, S. Vincent, S. Abadie, J.-P. Caltagirone, Three-dimensional Large Eddy Simulation of air entrainment under plunging breaking waves, *Coastal Eng.* 53 (2006) 631–655.
- [14] P. Lubin, H. Chanson, S. Glockner, Large Eddy Simulation of turbulence generated by a weak breaking tidal bore, *Environ. Fluid Mech.* 10 (5) (2010) 587–602.
- [15] P. Lubin, S. Glockner, O. Kimmoun, H. Branger, Numerical study of the hydrodynamics of regular waves breaking over a sloping beach, *Eur. J. Mech. B - Fluids* 30 (6) (2011) 552–564.
- [16] D. Brouilliot, P. Lubin, Numerical simulations of air entrainment in a plunging jet of liquid, *J. Fluids Struct.* 43 (2013) 428–440.
- [17] S. Cummins, M. Francois, D. Kothe, Estimating curvature from volume fractions, *Comput. Struct.* 83 (2005) 425–434.
- [18] S. Popinet, An accurate adaptive solver for surface-tension-driven interfacial flows, *J. Comput. Phys.* 228 (16) (2009) 5838–5866.
- [19] T. Abadie, J. Aubin, D. Legendre, On the combined effects of surface tension force calculation and interface advection on spurious currents within volume of fluid and level set frameworks, *J. Comput. Phys.* 297 (2015) 611–636.
- [20] M. Coquerelle, S. Glockner, A fourth-order accurate curvature computation in a level set framework for two-phase flows subjected to surface tension forces, *J. Comput. Phys.* 305 (2014).
- [21] T. Vinje, P. Brevig, Numerical simulation of breaking waves, *J. Adv. Water Resour.* 4 (1981) 77–82.
- [22] S. Abadie, J.-P. Caltagirone, P. Watremez, Mécanisme de génération du jet secondaire ascendant dans un déferlement plongeant, *C. R. Mécanique* 326 (1998) 553–559.
- [23] G. Chen, C. Khariif, S. Zaleski, J.J. Li, Two-dimensional Navier-Stokes simulation of breaking waves, *Phys. Fluids* 11 (1999) 121–133.
- [24] A. Iafrazi, Numerical study of the effects of the breaking intensity on wave breaking flows, *J. Fluid Mech.* 622 (2009) 371–411.
- [25] P. Lubin, Large Eddy Simulation of Plunging Breaking Waves, Université Bordeaux I, 2004 in English.
- [26] D.H. Peregrine, Breaking waves on beaches, *Annu. Rev. Fluid Mech.* 15 (1983) 149–178.

- [27] K.T. Kiger, J.H. Duncan, Air-entrainment mechanisms in plunging jets and breaking waves, *Annu. Rev. Fluid Mech.* 44 (2012) 563–596.
- [28] M.S. Longuet-Higgins, E.D. Cokelet, The deformation of steep surface waves on water – I. A numerical method of computation, *Proc. R. Soc. Lond. A* 350 (1976) 1–26.
- [29] E.D. Cokelet, Mechanics of Wave-Induced Forces on Cylinders, in: T. L. Shaw (Ed.), 1979 pp. 287–301.
- [30] D.H. Peregrine, E.D. Cokelet, P. McIver, The fluid mechanics of waves approaching breaking, in: *Proc. 17th Int. Conf. Coastal Eng.*, 1980, pp. 512–528.
- [31] M.S. Longuet-Higgins, Parametric solutions for breaking waves, *J. Fluid Mech.* 121 (1982) 403–424.
- [32] A.L. New, P. McIver, D.H. Peregrine, Computations of overturning waves, *J. Fluid Mech.* 150 (1985) 233–251.
- [33] D.A. Drazen, W.K. Melville, L. Lenain, Inertial scaling of dissipation in unsteady breaking waves, *J. Fluid Mech.* 611 (2008) 307–332.
- [34] D. Sharp, An overview of Rayleigh-Taylor instability, *Physica D* 12 (1) (1984) 3–18.
- [35] W.S. Saric, Görtler Vortices, *Annu. Rev. Fluid Mech.* 26 (1) (1994) 379–409.
- [36] M.S. Longuet-Higgins, On the disintegration of the jet in a plunging breaker, *J. Phys. Oceanogr.* 25 (10) (1995) 2458–2462.
- [37] M. Narayanaswamy, R.A. Dalrymple, An experimental study of surface instabilities during wave breaking, in: J.M. Smith (Ed.), *Proceedings of the ASCE 28th International Conference on Coastal Engineering*, Vol. 1, World Scientific, 2002, pp. 344–355.
- [38] Y. Watanabe, H. Saeki, R.J. Hosking, Three-dimensional vortex structures under breaking waves, *J. Fluid Mech.* 545 (2005) 291–328.
- [39] E. Levi, Longitudinal streakings in liquid currents, *J. Hydraul. Res.* 3 (2) (1965) 25–39.
- [40] A. Saruwatari, Y. Watanabe, D.M. Ingram, Scarifying and fingering surfaces of plunging jets, *Coastal Eng.* 56 (11–12) (2009) 1109–1122.
- [41] G. Liang, I. Mudawar, Review of mass and momentum interactions during drop impact on a liquid film, *Int. J. Heat Mass Transfer* 101 (2016) 577–599.
- [42] E.L. Andreas, J.B. Edson, E.C. Monahan, M.P. Rouault, S.D. Smith, The spray contribution to net evaporation from the sea: A review of recent progress, *72 (1–2) (1995) 3–52.*
- [43] F. Veron, Ocean spray, *Annu. Rev. Fluid Mech.* 47 (2015) 507–538.
- [44] F. Veron, C. Hopkins, E. Harrison, J. Mueller, Sea spray spume droplet production in high wind speeds, *39 (16) (2012).*
- [45] J.O. Hinze, Critical speeds and sizes of liquid globules, *Appl. Sci. Res. A1 (4) (1949) 273–288.*
- [46] J.O. Hinze, Fundamentals of the hydrodynamic mechanism of splitting in dispersion processes, *AIChE J.* 1 (3) (1955) 289–295.
- [47] J.O. Hinze, *Turbulence*, second ed., McGraw-Hill, 1975, p. 790.
- [48] M. Angelova, R.P. Barber, J. Wu, Spume drops produced by the wind tearing of wave crests, *29 (1999) 1156–1165.*
- [49] C.W. Fairall, M.L. Banner, W.L. Peirson, W. Asher, R.P. Morison, Investigation of the physical scaling of sea spray spume droplet production, *J. Geophys. Res.* 114 (C10) (2009).
- [50] E. Villermaux, B. Bossa, Single-drop fragmentation distribution of raindrops, *Nat. Phys.* 5 (9) (2009).
- [51] J.A. Mueller, F. Veron, A sea state-dependent spume generation function, *39 (2009) 2363–2372.*
- [52] M.P. Buckley, F. Veron, Structure of the airflow above surface waves, *J. Phys. Oceanogr.* 46 (5) (2016) 1377–1397.
- [53] R.J. Farahani, R.A. Dalrymple, Three-dimensional reversed horseshoe vortex structures under broken solitary waves, *Coastal Eng.* 91 (2014) 261–279.
- [54] P.D. LeClaire, F.C. Ting, Measurements of suspended sediment transport and turbulent coherent structures induced by breaking waves using two-phase volumetric three-component velocimetry, *Coast. Eng.* 121 (2017) 56–76.
- [55] K. Nadaoka, M. Hino, Y. Koyano, Structure of the turbulent flow field under breaking waves in the surf zone, *J. Fluid Mech.* 204 (1989) 359–387.
- [56] K.A. Brucker, T.T. O’Shea, D.G. Dommert, P. Adams, Three-dimensional simulations of deep-water breaking waves, in: *Proceedings of the 28th Symposium on Naval Hydrodynamics*, 2010.
- [57] E. Lamarre, An experimental study of air entrainment by breaking waves, Massachusetts Institute of Technology and the Woods Hole Oceanographic Institution, 1993.
- [58] G.B. Deane, M.D. Stokes, Air entrainment processes and bubble size distributions in the surf zone, *J. Phys. Oceanogr.* 29 (7) (1999) 1393–1403.
- [59] G.B. Deane, M.D. Stokes, Scale dependence of bubble creation mechanisms in breaking waves, *Nature* 418 (2002) 839–844.
- [60] G. Rojas, M.R. Loewen, Void fraction measurements beneath plunging and spilling breaking waves, *J. Geophys. Res.* 115 (C08001) (2010).
- [61] C.E. Blenkinsopp, J.R. Chaplin, Bubble size measurements in breaking waves using optical fiber phase detection probes, *IEEE J. Ocean. Eng.* 35 (2) (2010) 388–401.
- [62] C.E. Blenkinsopp, J.R. Chaplin, Void fraction measurements and scale effects in breaking waves in freshwater and seawater, *Coastal Eng.* 58 (2011) 417–428.
- [63] H.-J. Lim, K.-A. Chang, Z.-C. Huang, B. Na, Experimental study on plunging breaking waves in deep water, *J. Geophys. Res. Oceans* 120 (2015) 2007–2049.
- [64] O. Kimmoun, L. Brosset, G. Dupont, Experimental study of wave impacts on a corrugated ceiling, in: *Proc. 26th Int. Offshore and Polar Engng. Conf.*, 2016.